14th International Symposium on Turbulence and Shear Flow Phenomena (TSFP14)
Heidelberg, Germany, July 28-31, 2026

Integrated Optimization of Passive and Active Controls for Drag Reduction of an Axisymmetric Body

Wenlong Zhao
School of Mechanical Engineering
Shanghai Jiao Tong University
Shanghai 200240, China
School of Mechanical Engineering & Mechanics,
Eastern Institute of Technology,
Ningbo, Ningbo 315000, China
zwl123@sjtu.edu.cn

Guoming Deng
College of Urban Transportation and Logistics
Shenzhen Technology University
Shenzhen 518118, China
dengguoming@outlook.com

Yu Zhou*
School of Mechanical Engineering & Mechanics, Eastern Institute of Technology,
Ningbo, Ningbo 315000, China
yuzhou@eitech.edu.cn
*Corresponding author

ABSTRACT

This study proposes an artificial-intelligence-based virtual engineering technology for integrating passive control technique or shape optimization (SO) and active flow control (AFC) of an axisymmetric body to minimize its hydrodynamic drag, with a view to achieving superior control performance compared to SO only or AFC only or a superposition of SO and AFC. The methodology integrates a parameterization scheme with a Bayesian optimization algorithm. Hydrodynamic drag is evaluated using Reynolds-averaged Navier-Stokes (RANS) equations closed with the k-ω SST two-layer turbulence model. Preliminary results show that the integrated optimization of 18 control parameters (9 passive and 9 active) yields a maximum drag reduction (DR) of 32% and a net saving of energy (NSE) of 29%. In contrast, SO only results in a DR of 23%, while AFC only achieves a DR of 24% and a NSE of 21%. A superposition of SO and AFC leads to only 23% DR and 20% NSE. The finding demonstrates the great potential of the proposed technique to maximize the hydrodynamic performance of a high-speed vehicle, with implications for engineering applications.

INTRODUCTION

Control of flow separation from a bluff body is crucially important in various industrial applications, such as underwater vehicles and aircrafts. The separated flow forms a wake characterized by a low-pressure recirculation region surrounded by unsteady shear layers, which is closely related to the drag force or base pressure on the bluff body. Effective flow control or drag reduction (DR) therefore targets suppressing either separation or shear-layer instability or both.

Techniques for flow manipulation and DR broadly fall into two categories: passive and active controls. The former does not involve energy input, while the latter does. As such, we may for convenience refer the shape optimization (SO) of a vehicle as a passive technique. SO has been investigated since the 1970s (Pironneau 1973) and, after decades of development, has yielded substantial performance improvements owing to its effectiveness and ease of implementation. Active flow control (AFC) in contrast has attracted recently growing attention for its flexibility and adaptability to varying operating conditions. These two approaches have however been pursued separately in the past, for it is very difficult, if not impossible, to use conventional mathematics or optimization methods to solve the problem if the two are integrated. However, the emergence of machine learning or artificial intelligence (AI) control makes it possible to find the near-global optimal solutions of a problem involving dozens of control variables (Zhou et al. 2020; Zhang et al. 2023; Deng et al. 2024). Then, one important question arises. Can SO and AFC be integrated through AI-driven optimization and yield solutions, say in terms of DR and NSE of an underwater vehicle model, superior to those obtained from either SO or AFC or a superposition of both? If so, what are the physical mechanisms associated with the solutions?

To address the issues, we have developed an AI-driven optimization framework that integrate SO and surrogate-model-based AFC (Xi et al. 2024), based on which an axisymmetric body or a DARPA SUBOFF model is manipulated whose afterbody is replaced by a hemispherical geometry (Song et al. 2025). A total of 18 control parameters (9 passive and 9 active) is optimized. The methodology, results and discussion, and preliminary conclusions are presented in this paper.

METHODOLOGY

Numerical setup and validation

The axisymmetric model investigated in this study shown in figure 1(a), has a length of 1.24 m (L) and a diameter of 0.2 m (D). The geometry is parameterized using Non-Uniform Rational B-Splines (NURBS), with five adjustable control points located near the aft section to enable shape deformation (figure 1b). A three-dimensional body is generated by revolving the profile 360° about the x-axis. AFC is implemented via three jet slits placed at the aft end of the model, each with a width of 0.0075D (figure 1(c)).

Numerical simulations are conducted at a Reynolds number of 2.7×10^5, based on the free-stream velocity (U_∞ = 1.356 m/s) and the model diameter. The flow is solved using RANS equations coupled with the k-ω SST two-layer turbulence model in Siemens STAR-CCM+®. Convective terms are discretised using a second-order upwind scheme, whilst the pressure-velocity coupling is achieved using the SIMPLE algorithm.

A hybrid mesh consisting of hexahedral cells and prism layers is adopted, ensuring a dimensionless wall distance (y^+) in the range of 30 to 120. Local mesh refinement is applied near the body surface and in the wake region, resulting in a total of approximately 1.6 million cells (figure 2b). As shown in figure 3, the computational framework is validated by comparing the predicted pressure coefficient (C_p) distribution along the symmetry plane with results reported by Huang (1992) and Mitra et al. (2019). The numerical predictions show well agreement with the reference data, confirming the reliability of the computational framework.

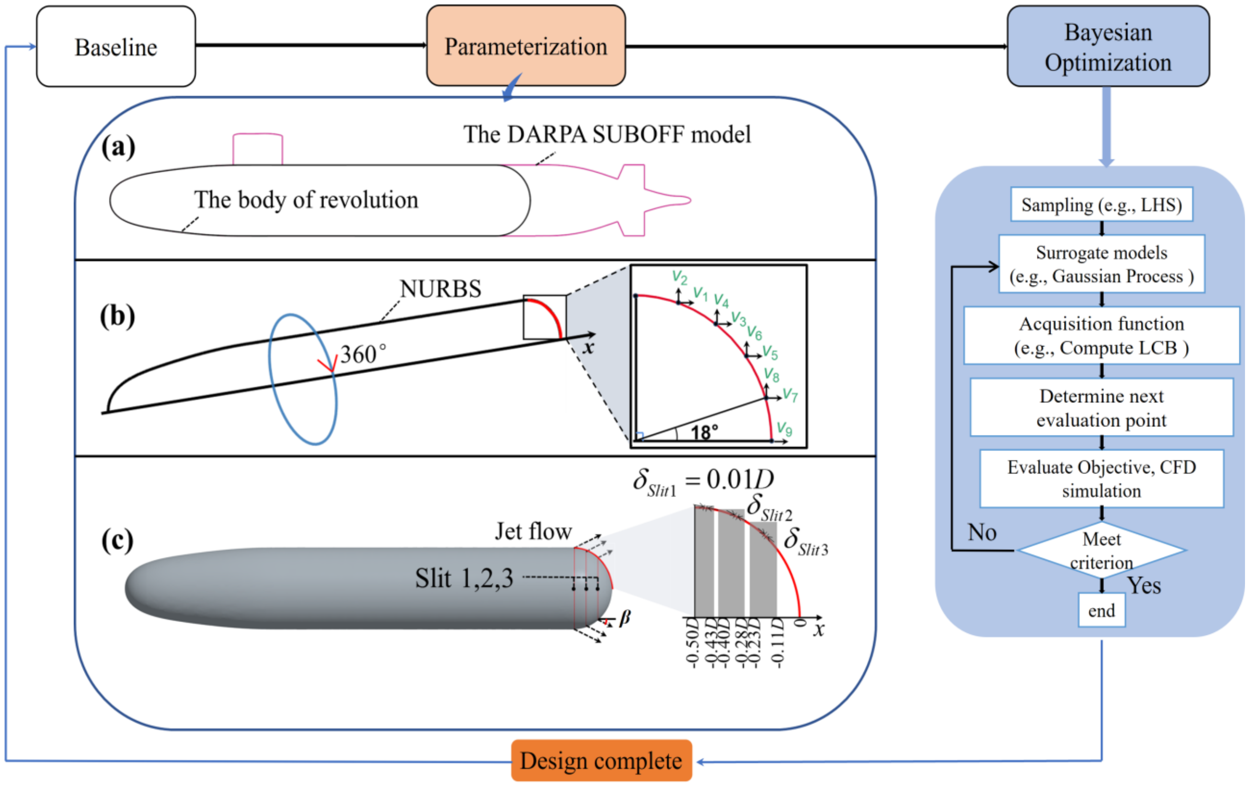

Figure 1. Flowchart of the proposed AI driven parameter-optimization framework and schematic of model parameterization. (a) profile curve; (b) NURBS-parameterized profile curve with the associated control-point set; (c) three-dimensional geometry and the layout

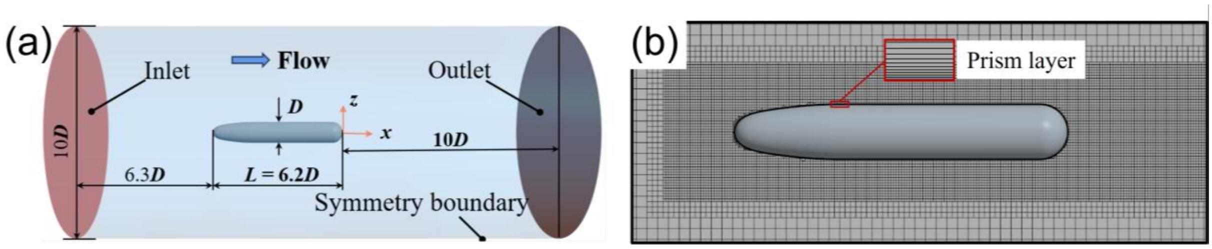

Figure 2. (a) Computation domain and geometry of the model. (b) Mesh distribution around the model.

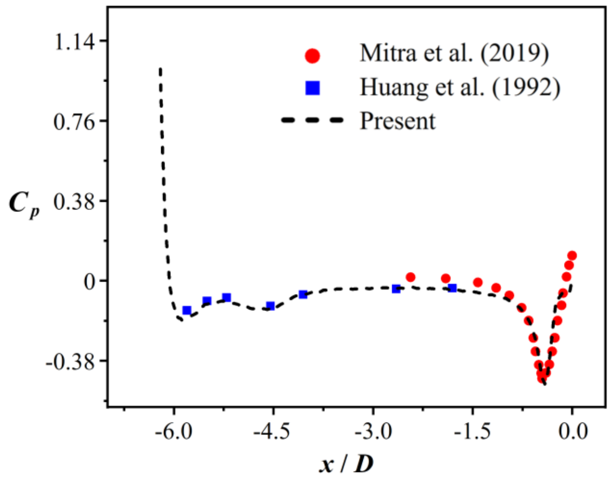

Figure 3. Comparison of pressure coefficient (C_p) along the centrelines in the symmetry plane between measurements and numerical simulation.

Integrated AI-based passive and active control.

The integrated AI-based passive and active control framework comprises three key components:

1) Geometric parameterization: As illustrated in figure 1(b), the geometry is parameterized using Non-Uniform Rational B-Splines (NURBS). Nine design variables (V_i, i = 1~9) are defined to control smooth shape deformations. The variables V_1 through V_8 are constrained within the range of ±0.05D, while V_9 ranges from 0 to 0.25D.

2) AFC parameterization: As illustrated in figure 1(c), three relocatable slits are deployed on the aft section of the model. The actuation of each jet (j = 1, 2, 3) is characterized by three control variables: velocity (U_j), jet angle (β_j), and jet location (P_j). The admissible range $\boldsymbol{B}$ of each control variable is defined in Table 1.

3) Parameter Optimization: Bayesian optimization is employed to explore the combined geometric and AFC parameter space, minimizing the net drag coefficient C_{dnet} = C_d + C_e, where C_d is the drag coefficient and C_e is the AFC energy penalty. Starting from initial samples ($\mathcal{D}_0$) evaluated via RANS simulations, a surrogate model is constructed and iteratively refined by selecting new candidates through an acquisition function. The total optimization budget is set to 15 times the dimensionality of the design variable vector $\boldsymbol{b}$; the detailed procedure is outlined in Algorithm 1.

Table 1. AFC control variables and their bounds.

Variable	Slit 1	Slit 2	Slit 3
U_j	[0, 2U_∞]	[0, 2U_∞]	[0, 2U_∞]
β_j	[0, 90°]	[-15°, 30°]	[-35°, 90°]
P_j	[-0.5D, -0.43D]	[-0.4D, -0.28D]	[-0.23D, -0.11D]

Two key components of Bayesian optimization are the choice of surrogate model and the acquisition strategy. Among various surrogate modelling approaches, Gaussian process (GP) regression is widely adopted due to its flexible non-parametric nature and its ability to model nonlinear black-box functions. Moreover, GP regression naturally provides a probabilistic quantification of predictive uncertainty, rendering it particularly well-suited for optimization problems involving high per-sample computational costs. In this work, the cost function (J) is modelled as a GP regression with a Matérn kernel. The predictive mean and standard deviation are denoted by $\mu(\boldsymbol{b})$ and $\sigma(\boldsymbol{b})$, respectively.

The acquisition function balances exploration (sampling regions of high uncertainty) and exploitation (refining regions of low predicted cost) to guide sampling toward the global minimizer. In this study, the lower confidence bound (LCB) acquisition function is adopted, where the hyperparameter κ, which controls the balance between exploration and exploitation, is set to 2:

$$a(\boldsymbol{b}) = \mu(\boldsymbol{b}) - \kappa\sigma(\boldsymbol{b}) \tag{1}$$

Algorithm 1 Bayesian optimization

1. Generate an initial set of sampling points $\mathcal{D}_0 = \{(\boldsymbol{b}_m, J_m)\}_{m=1}^{n_{init}}$.
2. Input: maximum iterations N_{max}.
3. while $n \leqslant N_{max}$ do:
   - Update the Gaussian Process model using the observed data $\mathcal{D}_{n_{init}+n-1}$.
   - Sample actuation: $\boldsymbol{b}_{n_{init}+n} = \arg\min_{\boldsymbol{b}\in\boldsymbol{B}} \alpha_{LCB}(\boldsymbol{b})$.
   - Evaluate the objective function: $J_{n_{init}+n}$
   - Augment the dataset: $\mathcal{D}_{n_{init}+n} = \mathcal{D}_{n_{init}+n-1} \cup \{(\boldsymbol{b}_{n_{init}+n}, J_{n_{init}+n})\}$.

   end while
4. Return the estimated global optimum: $\boldsymbol{b}^* = \arg\min_{\boldsymbol{b}\in\boldsymbol{B}} J(\boldsymbol{b})$.

RESULTS AND DISCUSSION

The DR relative to the baseline configuration can be obtained using the following expressions:

$$DR = \frac{C_{d0} - C_{d\_control}}{C_{d0}} \quad (2)$$

where C_{d0} and $C_{d\_control}$ represent the drag coefficients before and after optimization, respectively.

Following the energy input analyses by Zhang et al. (2023), the net saved energy (NSE) is evaluated based on the following formulation:

$$NSE = \frac{C_{d0} - C_{d\_control} - C_e}{C_{d0}} \quad (3)$$

$$C_e = \sum_{i=1,2,3} \frac{S_i U_i^3}{S_0 U_\infty^3} \quad (4)$$

Here, U_i, and S_i denote the velocity and area of jet slits, respectively. S_0 is the reference frontal area of the model, and U_∞ is the free-stream velocity.

Table 2. Performance comparison of different optimization strategies.

Optimization strategy	DR (%)	NSE (%)
SO-only	23	23
AFC-only	24	21
SO-AFC (coupled)	32	29
SO-AFC (superposition)	23	20

Table 2 and figure 4 summarize the results from four optimization strategies: SO-only, AFC-only, SO-AFC coupled and a superposition of SO-only and AFC-only. Among them, the integrated strategy delivers the best performance, achieving a maximum DR of 32% at the 308th iteration. After accounting for the energy consumption of AFC, the NSE remains substantial at 29%. In contrast, the SO-only strategy yields a peak DR of 23% at iteration 105, while the AFC-only strategy achieves a DR of 24% at iteration 88 (NSE = 21%). The superposition of the two individual strategies results in only 23% DR and 20% NSE. These findings demonstrate the superior effectiveness of the integrated optimization approach in enhancing DR.

Figure 5 illustrates the DR mechanisms by comparing the wake flow fields of the baseline and three optimized configurations. For the AFC-only strategy, control is achieved solely through the most downstream jet, oriented at a pitch angle of 20° relative to the local wall tangent. The observed wake modifications are primarily governed by the Coanda effect (Song et al., 2025; He et al., 2025), which delays boundary-layer separation and causes the recirculation region to contract in the spanwise direction. Meanwhile, the notably reduced velocity inside the recirculation region suggests that shear-layer entrainment is weakened, thereby suppressing momentum exchange between the recirculation region and the freestream and thereby promoting base pressure recovery.

For the SO-only strategy the optimized shape resembles a boat-tailed body, featuring mild surface curvature upstream of the separation point and a near-planar base. This configuration resulting in a streamwise elongation of the recirculation region. Similarly, the reduced velocity within the recirculation region indicates attenuated shear-layer entrainment and diminished momentum exchange with the freestream, contributing to an increase in base pressure.

The integrated optimization synergistically combines the strengths of both approaches: the Coanda effect delays boundary-layer separation, and the boat-tail geometry promotes a streamwise elongation of the recirculation region. The concurrent weakening of shear-layer entrainment from both mechanisms collectively contributes to a substantial pressure recovery on the model base, thereby reducing the drag.

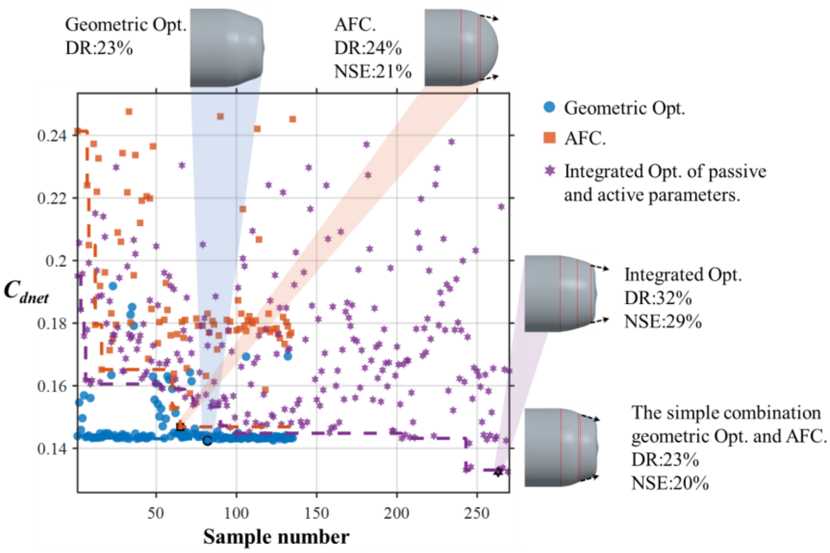

Figure 4. Comparison in the variation in C_{dnet} with iteration number n between the three control strategies.

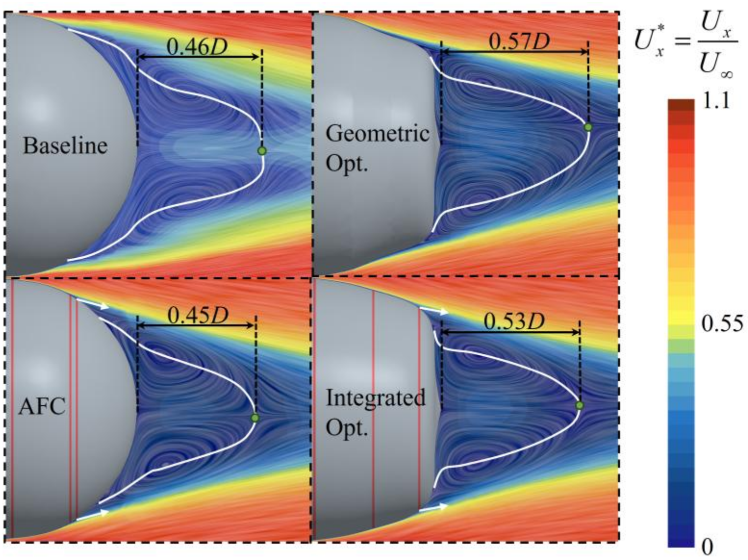

Figure 5. Wake velocity fields for the baseline case and the three control strategies. Saddle points are marked by green dots, the recirculation regions are delineated by white solid lines, and the jet directions are indicated by white arrows.

CONCLUSIONS

An AI-based virtual engineering method is proposed for the first time to integrate the SO and AFC of an axisymmetric body immersed in an axial flow, achieving a significant DR of 32% along with a substantial NSE of 29%. This method outperforms other three approaches, i.e., SO only (DR = 23%), AFC only (DR = 24%, NSE = 20%) or simple superposition of SO and AFC (DR = 23%, NSE = 20%). The results point to the great potential of the method in optimizing the hydrodynamic/aerodynamic performance of a high-speed vehicle.

The DR mechanisms are preliminarily investigated. For the AFC only, the control jets induce the Coanda effect and postpone flow separation, resulting in contracted recirculation region, reduced shear-layer entrainment and weakened momentum exchange between the recirculation and freestream regions. For the SO only, the boat-tail effect is produced, which prolongs the recirculation region and attenuates shear-layer entrainment. An in-depth understanding of the mechanisms for the integrated optimization of SO and AFC is underway.

ACKNOWLEDGEMENT

YZ wishes to acknowledge support given to him from NSFC through grants U24B2005 and U25A6006 and from NSF of Zhejiang Province through grant LZ25A020002.

REFERENCES

Pironneau O. (1973) On optimum profiles in Stokes flow. Journal of Fluid Mechanics 59(1), 117-128.

Song Y K, Chen J G, Zhou Y. (2025) Control of flow separation from an axisymmetric body using tangentially steady blowing jets. International Journal of Heat and Fluid Flow, 112, 109756.

Deng G M, Xi L C, Zhou Z, Liu H Y and Zhou Y (2024) AI-based shape optimization for drag reduction of a high speed train head/tail. Fluid-Structure-Sound Interactions and Control, Proceedings of the 6th Symposium on Fluid-Structure-Sound Interactions and Control (Eds. Daegyoum Kim, Kyung Chun Kim, Yu Zhou, Lixi Huang), pp. 225-232, Springer Berlin Heidelberg.

Xi L C, Deng G M, Zheng Z Y and Zhou Y (2024) Surrogate-model-based active drag reduction of high speed trains. Fluid-Structure-Sound Interactions and Control, Proceedings of the 6th Symposium on Fluid-Structure-Sound Interactions and Control (Eds. Daegyoum Kim, Kyung Chun Kim, Yu Zhou, Lixi Huang), pp. 267-272, Springer Berlin Heidelberg.

Huang, T., Liu, H. L., Groves, N., Forlini, T., Blanton, J. & Gowing, S. (1994) Measurements of flows over an axisymmetric body with various appendages in a wind tunnel: the DARPA SUBOFF experimental program. In Proceedings of the 19th Symposium on Naval Hydrodynamics, Seoul, Korea, 23–28 August 1992, National Academy Press.

Mitra, A., Panda, J., Warrior, H. (2019) The effects of free stream turbulence on the hydrodynamic characteristics of an AUV hull form. Ocean Engineering 174, 148-158.

He S, Zhou Y. (2025) Control and scaling of flow separation from a curved ramp using a pulsed jet. Journal of Fluid Mechanics, 1024: A17.

Zhang B F, Fan D W and Zhou Y. (2023) Artificial intelligence control of a low-drag Ahmed body using distributed jet arrays. Journal of Fluid Mechanics, 963, A3.

Zhou Y, Fan D, Zhang B F, Li R, Noack B R (2020) Artificial intelligence control of a turbulent jet. Journal of Fluid Mechanics. 897, A27 (46 pages).